PHYSICAL REVIEW B **69**, 035210 (2004)

Evolution of voids in Al^+-implanted ZnO probed by a slow positron beam

Z. Q. Chen, M. Maekawa, S. Yamamoto, and A. Kawasuso
Advanced Science Research Center, Japan Atomic Energy Research Institute, 1233 Watanuki, Takasaki, Gunma 370-1292, Japan

X. L. Yuan and T. Sekiguchi
Nanomaterials Laboratory, National Institute for Materials Science, 1-2-1 Sengen, Tsukuba, Ibaraki 305-0047, Japan

R. Suzuki and T. Ohdaira
National Institute of Advanced Industrial Science and Technology, 1-1-1 Umezono, Tsukuba, Ibaraki 305-8568, Japan
(Received 5 August 2003; revised manuscript received 28 October 2003; published 29 January 2004)

Undoped ZnO single crystals were implanted with aluminum ions up to a dose of $10^{15}Al^+/cm^2$. Vacancy defects in the implanted layers were detected using positron lifetime and Doppler broadening measurements with slow positron beams. It shows that vacancy clusters, which are close to the size of V_8, are generated by implantation. Postimplantation annealing shows that the Doppler broadening *S* parameter increases in the temperature range from 200 °C to 600 °C suggesting further agglomeration of vacancy clusters to voids. Detailed analyses of Doppler broadening spectra show formation of positronium after 600 °C annealing of the implanted samples with doses higher than 10^{14} Al^+/cm^2. Positron lifetime measurements further suggest that the void diameter is about 0.8 nm. The voids disappear and the vacancy concentration reaches the detection limit after annealing at 600–900 °C. Hall measurement shows that the implanted Al^+ ions are fully activated with improved carrier mobility after final annealing. Cathodoluminescence measurements show that the ultraviolet luminescence is much stronger than the unimplanted state. These findings also suggest that the electrical and optical properties of ZnO become much better by Al^+ implantation and subsequent annealing.

DOI: 10.1103/PhysRevB.69.035210 PACS number(s): 61.80.Jh, 78.70.Bj, 61.72.Ji

I. INTRODUCTION

Despite the fact that ZnO has been recognized as an excellent candidate for the production of short-wavelength optoelectronic devices,[1,2] its practical application is hindered due to a series of problems, such as the difficulty in the growth of high quality single crystals, and also the serious problem in *p*-type doping. Like many other wide band-gap semiconductors, there is a doping asymmetry[3] in ZnO. Contrary to the easy *n*-type doping, it is rather difficult to obtain *p*-type ZnO. Aluminum has been proved to be a good *n*-type dopant for ZnO, and Al-doped ZnO film has application in the transparent conduction electrode in solar cells.[4,5] Though nitrogen is expected to be a possible candidate of acceptor in ZnO,[6] only a few works have succeeded in reproducing *p*-type ZnO film through epitaxial growth.[7] Therefore, effective doping methods, which enable to control both *n*- and *p*-type conduction, should be established.

Besides the conventional doping method, ion implantation is also an effective way of selective doping in semiconductors. However, ion implantation results in severe damages to degrade the performance of semiconductor devices. Thus, systematic studies of implantation-induced defects and their annealing process are necessary to achieve successful doping by implantation method. There are a number of reports on the ion-implantation effects in ZnO,[8–18] and some of them reported the study of implantation-induced defects.[8–10,12,14,15,18] Positron annihilation spectroscopy (PAS) has emerged recently as a powerful method for the study of defects in semiconductors[19] because of its high sensitivity to vacancy-type defects with detection limit as low as 10^{15} cm^{-3}. This method has been applied to study grown-in as well as electron and proton irradiation induced defects in ZnO.[20–27] The energy-variable slow positron beam can especially be used for the study of depth profile of defects near the surface region.[28] In this paper, we investigated *n*-type doping in ZnO by implantation with aluminum ions. The introduction and annealing process of defects in the implanted ZnO were studied using positron annihilation spectroscopy combined with a slow positron beam. Electrical and optical properties of ZnO after implantation and annealing were also characterized by Hall and cathodoluminescence measurements.

II. EXPERIMENT

Undoped *n*-type ZnO single crystals with size of $10\times10\times0.5$ mm^3 and (0001) orientation were purchased from Scientific Production Company. The samples were first annealed at 900 °C in nitrogen ambient for 2 h to reduce grown-in defects.[27] A multiple-step Al^+ implantation with seven different ion energies ranging from 50 to 380 keV was performed at room temperature using a 400 keV ion implanter. The implantation sequence is from low to high energy. Ions were implanted to the Zn face of the samples. Figure 1 shows the implanted ion profile and vacancy profile calculated by TRIM.[29] A boxlike implantation profile is formed through such multiple-step implantation. The box layer thickness is around 550 nm. The vacancy also shows nearly homogeneous distribution in the box-shaped layer, but its breadth is a little smaller (~500 nm). The ion dose was varied from 10^{13} Al^+/cm^2 to 10^{15} Al^+/cm^2, and the actual dose at each energy was determined after multiplied with their respective ratio as shown in Fig. 1. Beam flux was

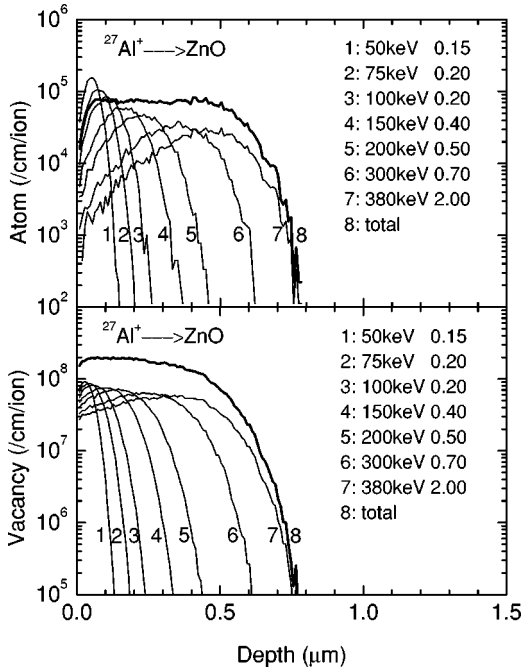

FIG. 1. TRIM simulation of the depth profile of (a) implanted ions and (b) introduced vacancies for the ZnO after multiple-step Al^+ implantation.

about 1.2×10^{12} $cm^{-2}\,s^{-1}$. After implantation, the samples were isochronally annealed in a nitrogen atmosphere in the temperature range from 200 °C to 900 °C for 30 min.

Defects in the implanted layer were probed by a slow positron beam in the energy range from 0.2 keV to 30 keV. Doppler broadening of annihilation radiation was measured using a high purity Ge detector with energy resolution of about 1.3 keV at 511 keV. The Doppler broadening spectra are characterized by the *S* parameter, which is defined as the ratio of the central region (511 ± 0.77 keV) to the total area of 511 keV annihilation peak. For the implanted sample with a dose of 10^{15} Al^+/cm^2, positron lifetime spectra were also recorded using a pulsed slow positron beam in National Institute of Advanced Industrial Science and Technology.[30] The incident positron energy was fixed at 7 keV, and total counts of $(3-6)\times10^6$ were collected in each lifetime spectrum. Hall measurements were conducted using the Van der Pauw method.[31] The ohmic contacts were fabricated by evaporating gold (with area ~1 mm^2) at the four symmetrical corners of samples after each final annealing process. Electrical connection to them was made with Al thread using a bonding machine. Cathodoluminescence was measured at room temperature using a modified scanning electron microscope[32] (TOPCON DS-130) in National Institute for Materials Science. A monochromator with grating of 100 lines/mm (Jobin Yvon HR320) and a charge coupled device were used for the detection of spectra. The slit width of the monochromator was 100 μm, which corresponds to a spectra resolution of 2.4 nm in wavelength. Detailed setup can be found in Ref. 32. The electron-beam energy and current for excitation were 5 kV and 1 nA, respectively. The acquisition time for each measurement was 5 s. All the samples were measured at once to assure the same beam condition during measurement. We

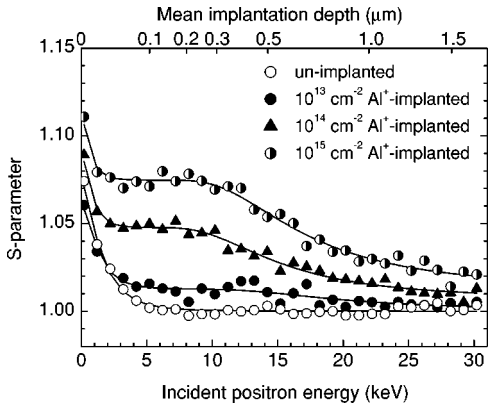

FIG. 2. *S-E* curves measured for the unimplanted and Al^+-implanted ZnO.

measured two different positions for each sample and found little difference between them, indicating that the result was highly repeatable.

III. RESULTS AND DISCUSSION

A. Positron annihilation measurements

1. Identification of defects in the as-implanted ZnO

Figure 2 shows the *S* parameter as a function of incident positron energy (*S-E* curve) for the ZnO before and after Al^+ implantation. In the unimplanted sample, *S* parameter decreases gradually with increasing incident positron energy and saturates at $E>5$ keV. This means that positrons annihilate in the deep bulk region at higher energies. The higher *S* parameter at lower energies ($E<3$ keV) can be explained by surface effects. All the *S* parameters are thus normalized to the value in the bulk region of the unimplanted sample.

After Al^+ implantation, the *S* parameter systematically increases with ion dose in the energy range of about 3–11 keV. This increase of *S* parameter shows the presence of vacancy defects after implantation, and the concentration of vacancy defects increases with ion dose. The plateau region at 3–11 keV reflects the homogeneous vacancy distribution due to the boxlike implantation profile though the *S* parameter gradually decreases above 11 keV.

In this work, the region sampled by positrons is divided into several layers. Considering the broad implantation profile and diffusion of positrons, the *S* parameter at incident positron energy *E* is then given by a linear combination of *S* parameters in each layer:

$$S(E)=S_S F_S(E)+\sum_{i=1}^{n} S_i F_i(E), \tag{1}$$

$$F_S(E)+\sum_{i=1}^{n} F_i(E)=1, \tag{2}$$

where S_S and S_i are the *S* parameters corresponding to the surface and *i*th layers, and the *S* parameter is assumed to be approximately the same within each layer. The measured

S-E curve is then analyzed using the VEPFIT program[33] by solving the following one-dimensional diffusion equation:

$$D_+ \frac{d^2}{dz^2} n(z) - \kappa_{eff}(z) n(z) + P(z,E) = 0, \tag{3}$$

where $n(z)$ is the positron density at distance z from the surface, $P(z,E)$ the positron implantation profile at given E, D_+ the positron diffusion coefficient, and the positron diffusion length $L_+(z)$ is given by $L_+(z) = \sqrt{D_+ / k_{eff}(z)}$. $k_{eff}(z)$ is the effective escape rate of positrons from the diffusion process. The effective escape rate is related to the concentration of implantation-induced defects by $k_{eff}(z) = \lambda_b + \mu C_d(z)$, where λ_b is the positron annihilation rate in the bulk state, μ the specific positron trapping rate, and C_d the defect concentration. The Makhov implantation profile for positrons is adopted:

$$P(z,E) = \frac{m z^{m-1}}{z_0^m} \exp\left[-\left(\frac{z}{z_0} \right)^m \right], \tag{4}$$

where $z_0 = \overline{z}/\Gamma(1+1/m)$, Γ is the Gamma function, $\overline{z}$ is the mean implantation depth of positrons, and $\overline{z} = AE^n/\rho$. m, n, and A are constants, and ρ is the material density. In this paper, the values of m, n, and A are 2.0, 1.6, and 4×10^{-6} g cm^{-2} keV$^{-1.6}$, respectively.[33]

For the unimplanted ZnO, the *S-E* curve is analyzed taking into account one layer in the VEPFIT program. That is, $S(E) = S_S F_S(E) + S_B F_B(E)$, where B denotes the deep bulk state. The solid lines in the figure represent the best fitting. The positron diffusion length is determined to be about 22 ± 11 nm. This is shorter than 52 nm for the Eagle Picher ZnO reported by Uedono *et al.*,[26] but is comparable to that of the ZnO film sample.[26] The short diffusion length might be due to the existence of some defects acting as scattering and trapping centers for positrons.

The *S-E* curves of the implanted samples were also analyzed in terms of one-dimensional diffusion equation, as shown above assuming one damage layer in addition to the surface and bulk layer. It is clear that the *S-E* data are well reproduced by the above model. The defect layer thickness is determined to be ≈ 500 nm, which is in good agreement with TRIM calculation. The positron diffusion length in the damage layer decreases continuously with increasing ion dose, and reaches 4 ± 1 nm at the highest dose because of the trapping of positrons at vacancy defects. The *S* parameter in the defect layer increases up to nearly 1.08 at the highest dose. Previous PAS study[25] showed that the increase of *S* parameter is rather small ($<1\%$) after 2 MeV electron irradiation in ZnO with a dose of 5×10^{18} cm^{-2}, which produces only simple defects such as monovacancies. Our detailed electron irradiation study[34] using 3 MeV electron up to a dose of 5×10^{18} cm^{-2} revealed that the specific *S* parameter for Zn monovacancy is ≈ 1.02 (2% higher than the bulk value before irradiation). Even after 3 MeV proton irradiation to a dose of 1.2×10^{18} cm^{-2}, which produces divacancies, the increase of *S* parameter is only about 3%.[22,23] Therefore it is obvious that Al^+ implantation produces large vacancy clusters. Such difference is due to the much heavier ion mass which causes more collision cascades as compared to electron and proton irradiation.

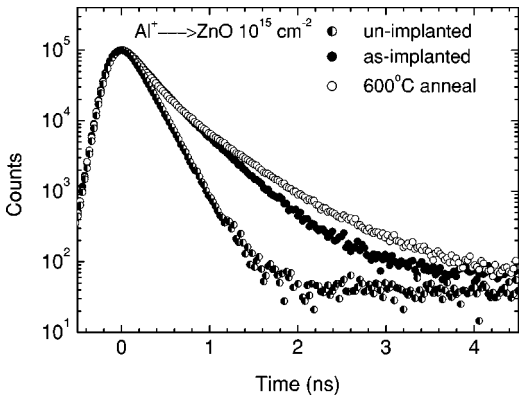

FIG. 3. Positron lifetime spectra measured for the ZnO before and after Al^+ implantation (10^{15} Al^+/cm^2) and 600 °C annealing. The incident positron energy is fixed at 7 keV.

To evaluate the size of these vacancy clusters more directly, we measured positron lifetime before and after Al^+ implantation with a dose of 10^{15} Al^+/cm^2 using a pulsed slow positron beam. The incident positron energy is 7 keV, which corresponds to the center of the damage area. The positron lifetime spectra are plotted in Fig. 3. They are analyzed using PATFIT program[35] based on a sum of several exponential decay terms:

$$L(t) = \sum_{i=1}^{n} \frac{I_i}{\tau_i} \exp\left(-\frac{t}{\tau_i} \right). \tag{5}$$

The lifetime spectrum of the unimplanted sample is fitted to a single exponential function with $\tau = 188 \pm 1$ ps. This is close to the lifetime of 181 ps determined through conventional lifetime measurements.[27] Though this lifetime is still longer than the previous bulk lifetime of ZnO [160–169 ps (Refs. 20, 25, and 26)], it is hardly reduced by further annealing. Thus, we consider this state as a standard for reference. After Al^+ implantation, the second lifetime component appears, which is about 377 ± 7 ps with intensity of $(66 \pm 3)\%$. This long lifetime is obviously due to positron trapping and annihilation at large vacancy clusters produced by implantation. The first lifetime is determined to be 195 ± 14 ps with intensity of $(34 \pm 3)\%$, which might be a weighted average of free and trapped positron lifetimes at small vacancies.

To confirm the PATFIT analysis based on discrete lifetime components, we extracted continuous positron lifetime distributions using CONTIN program[36] based on the Laplace inversion algorithm. The result is shown in Fig. 4. For the unimplanted sample, only one narrow peak centered at around 192 ps is seen. This is consistent with the above PATFIT analysis. After Al^+ implantation with a dose of 10^{15} Al^+/cm^2, two peaks are observed. The second peak is around 374 ps with an integrated intensity of about 66%. The first peak is around 210 ps. Thus, all these results show a good agreement with PATFIT analysis.

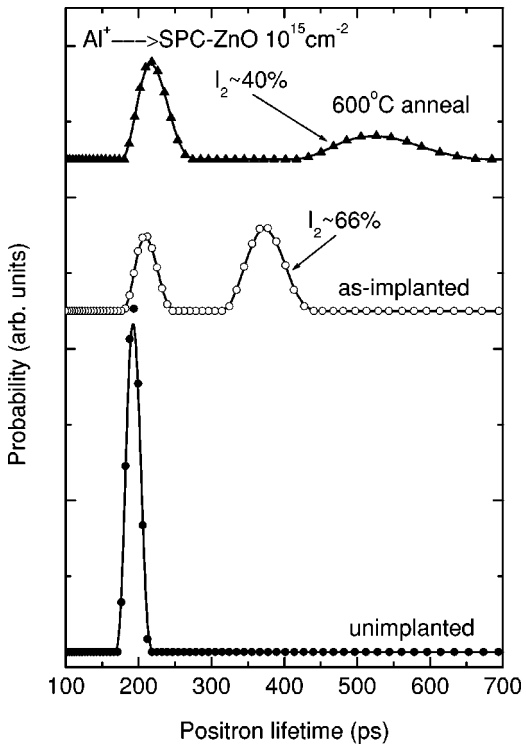

FIG. 4. Positron lifetime distribution measured for the ZnO before and after Al^+ implantation (10^{15} Al^+/cm^2) and 600 °C annealing. The incident positron energy is fixed at 7 keV.

We also calculated positron lifetime at various sizes of vacancy clusters in ZnO using the atomic superposition method.[37] Two approximations are made in the calculation.

(1) The short-range enhancement of the electron density at the positron is calculated using the semiconductor model proposed by Puska *et al.*[38] Beyond this range, the positron does not affect the electron structure.

(2) The lattice relaxation around the vacancy is not taken into account.

A supercell containing 64 Zn atoms and 64 O atoms is composed and the periodic boundary condition is used. This supercell is large enough for our calculation of vacancy clusters, as the positron wave function is found to be well localized within the supercell. The vacancy clusters are constructed by taking away the closest Zn-O pairs from the supercell to keep the minimum number of dangling bonds. For example, the configuration of V_6 ($3\text{-}V_{Zn}V_O$) is assumed to be so-called six-membered ring. The lattice constant of $a=0.325$ nm and $c=0.521$ nm for ZnO is used in the calculation. The calculated positron lifetimes are shown in Fig. 5 for different vacancy clusters. The V_{Zn} monovacancy is also presented. The calculated positron bulk lifetime in ZnO is about 158 ps. For V_8 ($4\text{-}V_{Zn}V_O$), the positron lifetime increases to about 350 ps, which corresponds to a ratio τ_d/τ_b of 2.2. As for our Al^+-implanted ZnO, the ratio τ_d/τ_b is around 2.1 using τ_b of about 181 ps.[27] Therefore, the size of the vacancy clusters might be close to V_8.

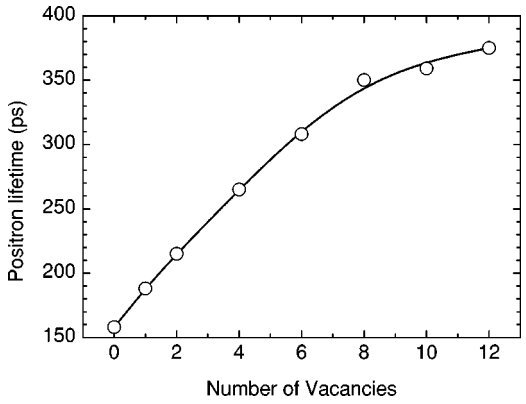

FIG. 5. Calculated positron lifetime at vacancy clusters in ZnO using atomic superposition method.

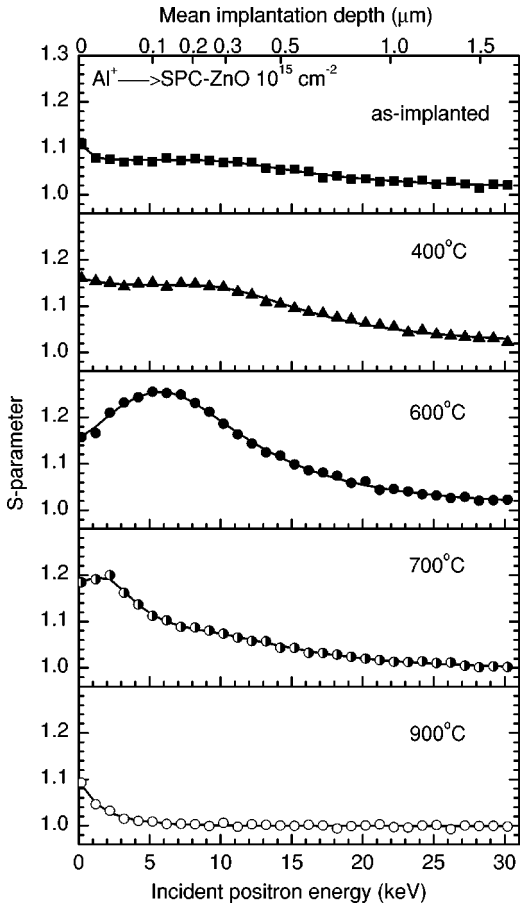

FIG. 6. Annealing behavior of the *S*-*E* curves measured for the Al^+-implanted ZnO with a dose of 10^{15} Al^+/cm^2.

2. Annealing of implantation-induced defects

Figure 6 presents some selected *S*-*E* curves for the sample implanted with a dose of 10^{15} Al^+/cm^2 and annealed at different temperatures. It is found that the *S* parameters in the implanted layer increase with annealing temperature, reach a maximum at 600 °C, then decrease and recover to the unimplanted level at 900 °C. The *S*-*E* curves were analyzed after each annealing step based on the above one-dimensional diffusion equation. Below 500 °C, the experimental *S*-*E* data are well reproduced considering one damage layer. On the

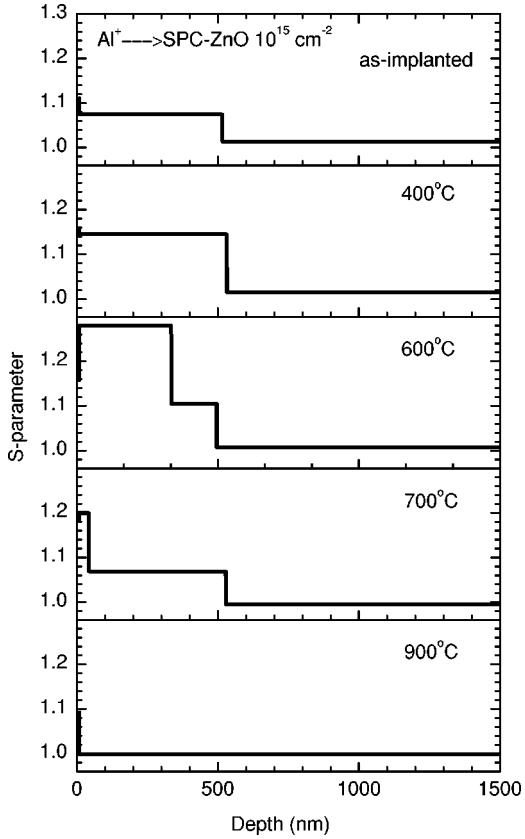

FIG. 7. Depth profile of *S* parameter for the Al^+-implanted ZnO with a dose of 10^{15} Al^+/cm^2 obtained from VEPFIT analysis. Two defect layers appear after annealing above 500 °C. The total damage layer thickness keeps unchanged during the annealing process.

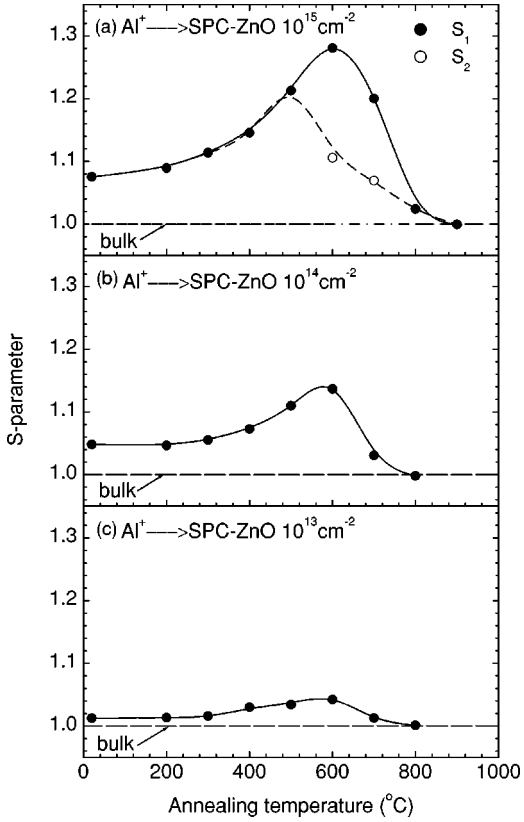

FIG. 8. *S* parameter in the defect layers as a function of annealing temperature for the Al^+-implanted ZnO. For the sample implanted with a dose of 10^{15} Al^+/cm^2, two defect layers appear after annealing at 600–700 °C. S_1 and S_2 are the *S* parameters in the first and second defect layer, respectively.

other hand, above 500 °C, two damage layers are needed. Solid lines in the figure represent thus obtained best fittings. Figure 7 shows the depth distributions of *S* parameters at the same annealing temperatures as in Fig. 6. At 600 °C, two defect layers appear. The first layer boundary is at about 335 nm, and that of the second layer is at about 500 nm. After 700 °C annealing, the first layer boundary decreases to about 42 nm, while the second layer boundary slightly increases to 528 nm. These two defect layers merge into one layer again after further annealing at 800 °C. At 900 °C, the defect layer disappears, indicating recovery of the implantation-induced defects which are seen by positrons. The total defect layer thickness does not show significant change during annealing until the full recovery of defects, i.e., it keeps at around 500 nm. For the other two implanted samples, the overall annealing behavior is nearly the same, i.e., only the magnitude of change is different. One difference is that no second defect layer is seen in these two samples through VEPFIT analysis.

Figure 8 shows the annealing behavior of *S* parameters in each defect layer as seen in Fig. 7 for all the implanted samples. The *S* parameter increases with temperature in the range from 200 °C to 600 °C, and then recovers gradually to the bulk value at 600–900 °C. The increase of *S* parameter at 200–600 °C indicates evolution from vacancy clusters to much larger vacancy agglomerates, and the subsequent decrease of *S* parameter indicates recovery of the implantation-induced vacancy defects. For the sample implanted with a dose of 10^{15} Al^+/cm^2, as mentioned above, there are two defect layers after annealing at 600–700 °C. The *S* parameter in the first layer is higher than that in the second layer. This is possibly due to the slightly lower vacancy concentration near the end of the implanted box layer as shown in Fig. 1. For the as-implanted sample, the *S* parameter is not sensitive to such small difference, so only one defect layer is seen by positrons. But after annealing at 600 °C, due to the agglomeration of vacancies, the vacancy size or concentration in the shallower region becomes larger or higher than that in the deeper region near the end of the box layer, and then the difference can be reflected by the *S* parameter. Further annealing at 700 °C causes decrease of *S* parameter and change of their respective layer thickness, which is due to the recovery of vacancies and redistribution of vacancy size. At 800 °C, the vacancy size or concentration in the two layers decreases to the same level, so again only one layer is obtained from fitting.

It is notable that *S* parameters increase to rather high value after annealing of the implanted samples with higher doses ($\geqslant 10^{14}$ Al/cm^2). At 600 °C, *S* parameter reaches 1.28 and 1.14 at doses of 10^{15} Al^+/cm^2 and 10^{14} Al^+/cm^2, respectively. This large *S* parameter might be due to formation of positronium (Ps) atoms, as suggested by several authors.[39] The Ps atom is the bound state of a positron with an

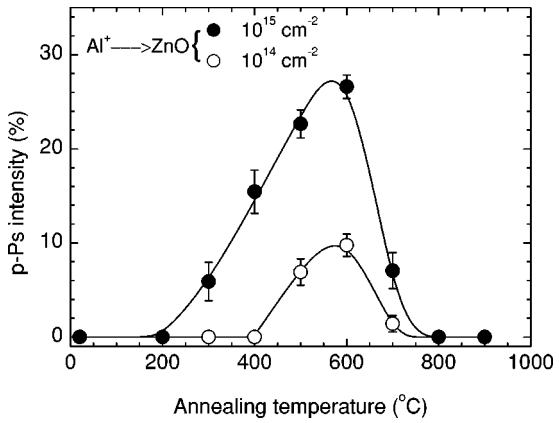

FIG. 9. p-Ps intensity obtained from the fitting of the integrated Doppler spectra (5–9 keV) for the Al^+-implanted ZnO as a function of annealing temperature.

electron.[40] It will be formed in the open spaces of porous materials[41] where the electron density is sufficiently low. According to the spin orientation of the electron and positron, Ps has two states: para-Positronium (p-Ps, the singlet spin state) and ortho-Positronium (o-Ps, the triplet spin state). The ratio of p-Ps to o-Ps formation probability is 1:3 in a vacuum. p-Ps mostly undergoes self-annihilation, i.e., the positron annihilates with its own electron by emitting two γ rays, while o-Ps annihilates into three γ rays in vacuum and two γ rays in media. Because p-Ps has nearly zero momentum, its self-annihilation will contribute a very narrow peak to the Doppler broadening spectrum. Therefore, the large S parameter may be attributed to p-Ps self-annihilation.

The integrated Doppler broadening spectra at energy range of 5–9 keV (mean positron implantation range of 100–250 nm) were analyzed by multi-Gaussian fitting using the ACARFIT program.[35] This method was proved to be successful by Dlubek *et al.*[42] in the study of positronium in polymers. Indeed, we examined the accuracy of this method by measuring a series of polymers and an amorphous SiO_2 using both Doppler broadening and conventional positron lifetime measurements. The discrepancy of p-Ps intensity obtained from Doppler broadening spectrum is less than 2% as compared to that from positron lifetime measurements. The background of the spectrum was subtracted using the method proposed by Mogensen,[40] i.e., $B_i = B_R + (B_L - B_R)A_i/A_t$, where A_i is the area of the peak above the ith channel and A_t the total area of 511 keV peak. B_L and B_R are the average background on the left- and right-hand sides of the peak, respectively. For the unimplanted and as-implanted samples, only two Gaussian components with full width at half maximum (FWHM) of 2.9 keV and 5.0 keV are resolved. They can be attributed to valance and core electron momentum distribution, respectively. Al^+ implantation does not change the width of each component, but only causes change in their respective intensities. For the samples implanted with doses higher than 10^{14} Al^+/cm^2 and annealed at 600 °C, however, three Gaussian fitting becomes necessary. A very narrow component with 1.5 keV in FWHM appears. This narrow component might be due to p-Ps self-annihilation.

Figure 9 shows the p-Ps intensity as a function of annealing temperature for the implanted ZnO samples. For the sample implanted with a dose of 10^{14} Al^+/cm^2, formation of p-Ps starts at around 500 °C, and its intensity increases to $\approx$10% at 600 °C. While for the sample with a dose of 10^{15} Al^+/cm^2, p-Ps formation occurs at 300 °C, and its intensity increases to about 26% after 600 °C annealing. The p-Ps intensity decreases after further annealing and finally attains zero at 800 °C for both of the samples. No p-Ps formation is found in the sample implanted with a dose of 10^{13} Al^+/cm^2.

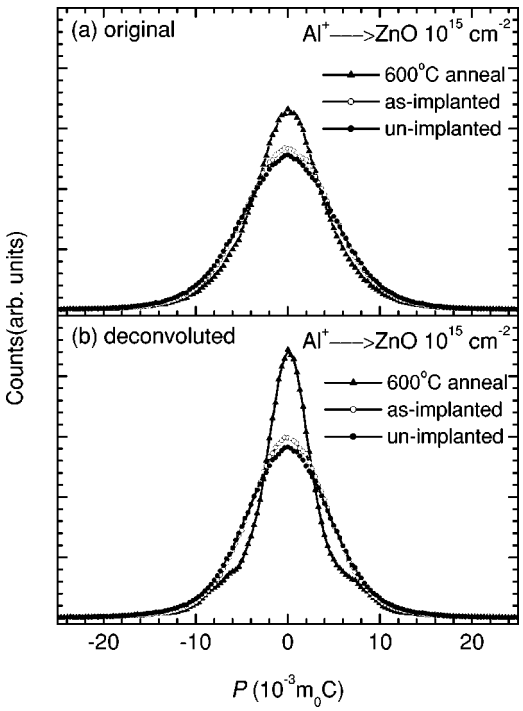

FIG. 10. (a) Original and (b) deconvoluted Doppler broadening spectra for the ZnO before and after Al^+ implantation (10^{15} Al^+/cm^2) and 600 °C annealing. The original spectrum is obtained by summing of the spectra at energy of 5–9 keV. The appearance of a narrow component after implantation and annealing indicates formation of p-Ps.

We also examined the shape of the integrated Doppler broadening spectra measured before and after implantation with a dose of 10^{15} Al^+/cm^2. The Doppler broadening spectrum can be expressed as

$$N(E) = \int_{-\infty}^{+\infty} R(E-E')D(E')dE', \tag{6}$$

where $D(E)$ is the real Doppler broadening spectrum, $R(E)$ is the energy resolution of the instrument, and $N(E)$ is the measured spectrum. Due to the instrument resolution, fine structures in the Doppler spectrum are likely to be smeared out. Thus, we deconvoluted the Doppler broadening spectra by using a Gaussian-type energy resolution function with FWHM of 1.3 keV. A point by point deconvolution method was used. Details of the deconvolution process were reported in Ref. 43. Both original and deconvoluted spectra are plotted in Fig. 10 for the samples before and after implantation and subsequent annealing at 600 °C. After implantation, the

central low momentum part shows some increase, which can be attributed to the reduced positron annihilation rate with high-momentum core electrons at vacancy clusters. After 600 °C annealing, the central part increases abruptly. This can be more clearly seen from the deconvoluted spectrum in Fig. 10(b). There, a very narrow component is superimposed to the broader (valence electron) peak. This narrow peak probably originates from p-Ps self-annihilation since it has nearly zero momentum.

The detection of p-Ps formation indicates also formation of o-Ps. From the analysis of the Doppler broadening spectra as a function of positron energy, we did not detect 3-γ annihilation of o-Ps in vacuum due to its diffusion to the sample surface. Therefore, we can assume that o-Ps is formed and trapped in large voids or open spaces in the implanted region, and annihilates into two γ rays. So the p-Ps intensity reflects information about the number of voids or porosity in the damage layer. As shown in Fig. 9, the number of voids first shows increase after annealing below 600 °C, and then decreases quickly with increasing annealing temperature, and finally disappears at 800 °C.

The positron lifetime measurement gives us direct evidence of Ps formation. After 600 °C annealing of the Al^+-implanted sample with a dose of 10^{15} Al^+/cm^2, the second positron lifetime component from PATFIT analysis increases to 446 ± 21 ps with intensity of (49 ± 1)%, and also a long lifetime of about 930 ± 120 ps with small intensity of (5 ± 2)% appears. However, CONTIN analysis shows only two peaks, but the second lifetime increases to around 530 ps with intensity of about 40%, and it becomes rather broad. The difference between PATFIT and CONTIN analysis might be due to the broad lifetime distribution. PATFIT analysis always tries to separate continuous lifetimes into discrete components, especially when the lifetime distribution expands in wide range. Actually if we use only two-component analysis by PATFIT, the result is then in agreement with CONTIN analysis, but the variance of fitting becomes worse. Therefore, in this case CONTIN analysis provides more reliable results. Because the average lifetime of this component is longer than 500 ps, this peak is apparently due to the annihilation of o-Ps. The wide o-Ps lifetime distribution indicates that after implantation and annealing, various sizes of voids are generated.

Considering both positron lifetime and Doppler broadening analyses, however, we find that the ratio of p-Ps to o-Ps intensity deviates from 1:3. For example, for the implanted sample with a dose of 10^{15} Al^+/cm^2, after 600 °C annealing the p-Ps intensity from Doppler broadening measurement is about 26%, while the o-Ps intensity from the lifetime measurement is only 40%. The ratio of p-Ps to o-Ps intensity increases to about 2:3. This is possibly due to the spin conversion of o-Ps caused by some paramagnetic centers on the surface of the voids.[44] Some of the o-Ps will then convert to p-Ps. The impurities, oxygen, and implanted aluminum are the possible paramagnetic centers. Our electron-spin-resonance measurements indeed show very high concentration of paramagnetic centers in the as-grown ZnO samples. This confirms that spin conversion of o-Ps is possible. The spin flip of o-Ps not only decreases o-Ps intensity (thereby increases p-Ps intensity), but also shortens o-Ps lifetime.[44] This is the reason for the short o-Ps lifetime in our sample. Using the same numerical calculation procedure as done by Dannefaer *et al.*,[44] we obtain the o-Ps pickoff annihilation rate $\lambda_{\text{pick-off}}$ to be about 0.68 ns^{-1} for the sample implanted with a dose of 10^{15} Al^+/cm^2 and annealed at 600 °C. So the o-Ps pickoff lifetime is about 1.48 ns. The void diameter can thus be obtained using the Tao-Eldrup relationship:[45,46]

$$\lambda_{\text{pick-off}}=2\left[1-\frac{R_0-\Delta R}{R_0}+\frac{1}{2\pi}\sin\left(2\pi\frac{R_0-\Delta R}{R_0}\right)\right], \quad (7)$$

where R_0 is the void radius, ΔR is the electron layer thickness, which is about 0.166 nm.[45,46] The average void diameter is then estimated to be about 0.8 nm.

All the above results confirm that the large increase of *S* parameter after annealing of the high dose implanted sample is due to positronium formation in large voids with an average diameter of about 0.8 nm. These large voids are formed due to the agglomeration of vacancies during annealing. Further annealing above 600 °C results in the recovery of these large voids. The number of voids formed after annealing depends on the implantation dose. For the sample implanted with the lowest dose (10^{13} Al^+/cm^2), the increase of *S* parameter is very small, and even after annealing, it increases only to about 1.04. No p-Ps peak is observed either. This means that no large voids are formed during implantation or after annealing, or their concentration is rather low.

The Ps intensity is closely related to the porosity of materials. For the implanted sample with the highest dose, the total Ps intensity ($I_{\text{o-Ps}}+I_{\text{p-Ps}}$) amounts to 66% after 600 °C annealing. This means that the implanted layer has transformed to highly porous structure. For a comparison, we measured an amorphous SiO_2, and the total Ps intensity is around 89%. The size of the void in our implanted ZnO sample is also close to that in the amorphous SiO_2 (o-Ps lifetime 1.58 ns, corresponding to a void diameter of 0.82 nm). Such comparison suggests that Al^+ implantation causes severe damage to ZnO and may even cause amorphization at higher dose ($>10^{14}$ Al^+/cm^2). However, previous studies[9,10,15] showed that amorphization in ZnO by ion implantation was rather difficult due to the effective dynamic annealing process. Sonder *et al.*[10] did not observe complete amorphous region in Bi, Mn, and Cr implanted ZnO with ion energy of 93–120 keV and ion dose up to $7\times10^{15}/cm^2$. Kucheyev *et al.*[15] also reported that amorphization was difficult for most of the ions. Therefore, at this moment, we cannot confirm whether amorphization occurs or not in our Al^+-implanted layer. Further experiments adopting other characterization methods are needed to solve this problem.

Our positron annihilation measurements show that complete recovery of vacancy defects occurs at 900 °C for high dose implanted sample and 800 °C for low dose implanted sample. This can be reflected by the recovery of *S* parameters shown in Fig. 8, which approach to that of the unimplanted bulk state after final annealing. The annealing temperature is a little lower than that reported by previous study,[10] which is around 1000 °C. There are several reasons for this difference. First, positron is mainly sensitive to vacancy-type de-

TABLE I. Hall measurements of sheet resistance R_S, free carrier concentration n_e, carrier mobility μ, and conduction type in the as-grown and Al^+-implanted ZnO after annealing.

Sample	R_S ($\Omega/\square$)	n_e (cm^{-3})	μ ($cm^2\,V^{-1}\,s^{-1}$)	Type
As-grown	3.3×10^5	5.7×10^{12}	66	*n*
As-grown + 900 °C	4950	3.6×10^{14}	70	*n*
10^{15} Al^+/cm^2 + 900°C	8.6	8.6×10^{19}	167	*n*

fects, while previous studies use Rutherford backscattering/channeling method, which detects mainly interstitial-type defects or impurities. Therefore the annealing behavior might be different for different types of defect. Second, the annealing behavior also depends on the implant and annealing condition. Much heavier ions (Bi, Mn, and Cr) and higher doses ($7\times10^{15}/cm^2$) were used in the previous study, and the annealing time is also shorter (15 min).[10] Therefore, a lower annealing temperature in our study is possible. Actually we have also performed implantation with other ions such as O^+ and N^+, and we found completely different annealing behavior of the implantation-induced defects.

B. Electrical characterization

The results of Hall measurements for the unimplanted and Al^+-implanted samples are listed in Table I. The repeated measurements show that all the data are reproducible, and hence are reliable. All the samples show *n*-type conductivity. For the as-grown sample, the sheet resistance is rather high ($3.3\times10^5\Omega/\square$). After 900 °C annealing, the sheet resistance decreases by nearly two orders of magnitude to about 5000 $\Omega/\square$. This might be due to reduction of acceptor-type defects such as V_{Zn}, or production of donor-type defects, such as oxygen vacancy V_O or Zn interstitial Zn_i. After Al^+ implantation with a dose of 10^{15} Al^+/cm^2 and annealing at 900 °C, the sheet resistance decreases abruptly to about 8.6 $\Omega/\square$. Assuming implanted layer thickness of 500 nm from TRIM calculation, the electron concentration increases to 8.6×10^{19} cm^{-3}, comparable to the implanted Al^+ concentration ($\sim7.5\times10^{19}$ cm^{-3} from TRIM calculation). This suggests that all the implanted aluminum ions are activated as donors after annealing. It is also interesting to note that the electron mobility increases from 70 $cm^2V^{-1}\,s^{-1}$ before implantation to 167 $cm^2\,V^{-1}\,s^{-1}$ after Al^+ implantation and annealing, indicating improved crystal quality. This might be due to the reduction of defects which exist in the as-grown ZnO and act as scattering centers.

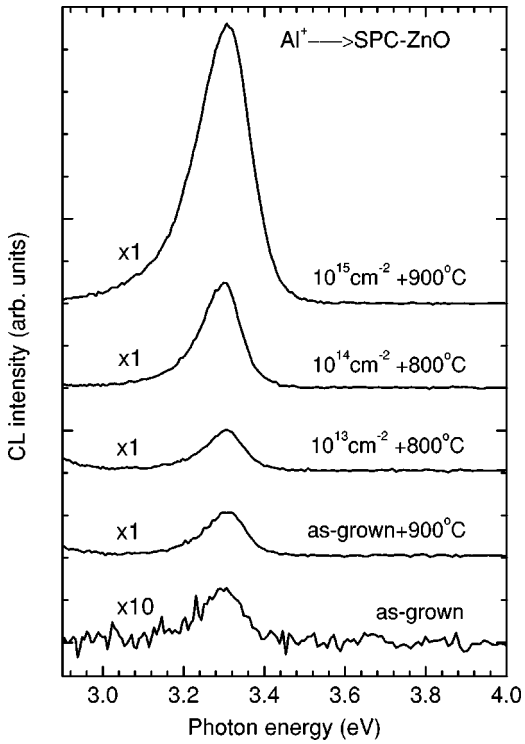

FIG. 11. Cathodoluminescence spectra measured at room temperature for the ZnO samples before and after Al^+ implantation and annealing.

C. Optical measurements

Figure 11 shows the result of cathodoluminescence measurements for the ZnO samples before and after implantation and annealing. In this paper we mainly considered the ultraviolet (UV) emission, which is attributed to the radiative recombination of free excitons.[47] This UV emission is closely related to the crystal quality of ZnO. For the as-grown ZnO, the UV emission is rather weak due to the existence of large amount of defects acting as nonradiative recombination centers. After 900 °C annealing, these defects in the as-grown sample are reduced,[27] and thus UV emission is enhanced. After Al^+ implantation with a dose of 10^{13} Al^+/cm^2 and 800 °C annealing, the UV emission peak has nearly the same height as that of the as-grown + 900 °C annealed sample. This indicates that all the implantation-induced defects are removed by 800 °C annealing. When the implantation dose increases to 10^{14} Al^+/cm^2, however, the UV emission is further enhanced. After implantation with a dose of 10^{15} Al^+/cm^2 and subsequent annealing at 900 °C, the height of UV emission is about 60 times greater as compared to the as-grown sample. This means that after Al^+ implantation and annealing, the ZnO crystal quality is fairly improved, in good agreement with the increase of electron mobility as shown by Hall measurements. However, further experiments are still needed to confirm this conclusion.

IV. CONCLUSION

Al^+-implantation-induced defects were studied by using a slow positron beam. The implantation introduces vacancy clusters. During annealing process, agglomeration of vacan-

cies into voids (200–600 °C) and annealing of voids (600–900 °C) take place, which is evidenced by positronium formation. The implantation-induced defects are under the detection limit after the ultimate annealing. Hall measurement shows that the implanted aluminum impurities are fully activated as donors, and the electron mobility is improved as compared to the only heat-treated sample. Cathodoluminescence measurements also show that the UV luminescence intensity becomes much stronger. Thus the ZnO crystal quality is improved after Al^+ implantation.

ACKNOWLEDGMENTS

The authors would like to thank Professor M. J. Puska for providing them the computer program to calculate theoretical positron lifetime. A fruitful discussion with Dr. Z. Tang about positron lifetime calculation was also acknowledged. This work was partly supported by the Nuclear Energy Generic Crossover Research Project promoted by Ministry of Education, Culture, Sports, Science and Technology of Japan.

[1] D.C. Look, D.C. Reynolds, J.R. Sizelove, R.L. Jones, C.W. Litton, G. Cantwell, and W.C. Harsch, Solid State Commun. **105**, 399 (1998).
[2] Y. Chen, D. Bagnall, and T. Yao, Mater. Sci. Eng., B **75**, 190 (2000).
[3] S.B. Zhang, Su-Huai Wei, and Alex Zunger, J. Appl. Phys. **83**, 3192 (1998).
[4] J. Hu and R.G. Gordon, J. Appl. Phys. **71**, 880 (1992).
[5] A.V. Singh, R.M. Mehra, Nuttawuth Buthrath, Akihiro Wakahara, and Akira Yoshida, J. Appl. Phys. **90**, 5661 (2001).
[6] A. Kobayashi, O.F. Sankey, and J.D. Dow, Phys. Rev. B **28**, 946 (1983).
[7] D.C. Look, D.C. Reynolds, C.W. Litton, R.L. Jones, D.B. Eason, and G. Cantwell, Appl. Phys. Lett. **81**, 1830 (2002).
[8] B.W. Thomas and D. Walsh, J. Phys. D **6**, 612 (1973).
[9] C.W. White, L.A. Boatner, P.S. Sklad, C.J. McHargue, S.J. Pennycook, M.J. Aziz, G.C. Farlow, and J. Rankin, in *Beam-Solid Interactions and Transient Processing*, edited by Michael O. Thompson, S. Thomas Picraux, and James S. Williams, Mater. Res. Soc. Symp. Proc. 74 (Materials Research Society, Pittsburgh, 1987), p. 357.
[10] E. Sonder, R.A. Zuhr, and R.E. Valiga, J. Appl. Phys. **64**, 1140 (1988).
[11] S. Kohiki, M. Nishitani, and T. Wada, J. Appl. Phys. **75**, 2069 (1994).
[12] F.D. Auret, S.A. Goodman, M. Hayes, M.J. Legodi, H.A. van Laarhoven, and D.C. Look, Appl. Phys. Lett. **79**, 3074 (2001); J. Phys.: Condens. Matter **13**, 8989 (2001).
[13] M. Komatsu, N. Ohashi, I. Sakaguchi, S. Hishita, and H. Haneda, Appl. Surf. Sci. **189**, 349 (2002).
[14] S.O. Kucheyev, P.N.K. Deenapanray, C. Jagadish, J.S. Williams, M. Yano, K. Koike, S. Sasa, M. Inoue, and K. Ogata, Appl. Phys. Lett. **81**, 3350 (2002).
[15] S.O. Kucheyev, J.S. Williams, C. Jagadish, J. Zou, C. Evans, A.J. Nelson, and A.V. Hamza, Phys. Rev. B **67**, 094115 (2003).
[16] D.-C. Park, I. Sakaguchi, N. Ohashi, S. Hishita, and H. Haneda, Appl. Surf. Sci. **203-204**, 359 (2003).
[17] U. Wahl, E. Rita, J.G. Correia, E. Alves, and J.P. Araújo, Appl. Phys. Lett. **82**, 1173 (2003).
[18] T. Monteiro, C. Boemare, M.J. Soares, E. Rita, and E. Alves, J. Appl. Phys. **93**, 8995 (2003).
[19] R. Krause-Rehberg and H.S. Leipner, *Positron Annihilation in Semiconductors, Defect Studies*, Springer Series in Solid-State Sciences Vol. 127 (Springer, Berlin, 1999).
[20] R.M. de la Cruz, R. Pareja, R. González, L.A. Boatler, and Y. Chen, Phys. Rev. B **45**, 6581 (1992).
[21] N. Tomiyama, M. Takenaka, and E. Kuramoto, Mater. Sci. Forum **105-110**, 1281 (1992).
[22] W. Puff, S. Brunner, P. Mascher, and A.G. Balogh, Mater. Sci. Forum **196-201**, 333 (1995).
[23] S. Brunner, W. Puff, P. Mascher, A.G. Balogh, and H. Baumann, Mater. Sci. Forum **258-263**, 1419 (1997).
[24] S. Brunner, W. Puff, P. Mascher, and A.G. Balogh, in *Microstructural Process in Infrared Materials*, edited by S. J. Zinkle, G. Lucas, R. Ewing, and J. Williams, Mater. Res. Soc. Symp. Proc. 540 (Materials Research Society, Pittsburgh, 1999), p. 207.
[25] S. Brunner, W. Puff, A.G. Balogh, and P. Mascher, Mater. Sci. Forum **363-365**, 141 (2001).
[26] A. Uedono, T. Koida, A. Tsukazaki, M. Kawasaki, Z.Q. Chen, S.F. Chichibu, and H. Koinuma, J. Appl. Phys. **93**, 2481 (2003).
[27] Z.Q. Chen, S. Yamamoto, M. Maekawa, A. Kawasuso, X.L. Yuan, and T. Sekiguchi, J. Appl. Phys. **94**, 4807 (2003).
[28] P.G. Coleman, *Positron Beams and their Applications* (World Scientific, Singapore, 2000).
[29] J.P. Biersack and L.G. Haggmark, Nucl. Instrum. Methods **174**, 257 (1980).
[30] R. Suzuki, T. Ohdaira, and T. Mikado, Radiat. Phys. Chem. **58**, 603 (2000).
[31] L.J. Van der Pauw, Philips Res. Rep. **13**, 1 (1958).
[32] T. Sekiguchi and K. Sumino, Rev. Sci. Instrum. **66**, 4277 (1995).
[33] A. van Veen, H. Schut, J. de Vries, R.A. Hakvoort, and M.R. Ijpma, in *Positron Beams for Solids and Surfaces*, edited by Peter J. Schultz, Guiti R. Massoumi, and Peter J. Simpson, AIP Conf. Proc. No. 218 (AIP, New York, 1990), p. 171.
[34] Z.Q. Chen, M. Maekawa, and A. Kawasuso (unpublished).
[35] P. Kirkegaard, N.J. Pederson, and M. Eldrup, Risø National Laboratory, DK-4000 Roskilde, Denmark, 1989.
[36] R.B. Gregory and Y. Zhu, Nucl. Instrum. Methods Phys. Res. A **290**, 172 (1990).
[37] M.J. Puska and R.M. Nieminen, J. Phys. F: Met. Phys. **13**, 333 (1983).
[38] M.J. Puska, S. Makinen, M. Manninen, and R.M. Nieminen, Phys. Rev. B **39**, 7666 (1989).
[39] A. Van Veen, H. Schut, and P.E. Mijnarends, in *Positron Beams and Their Applications* (Ref. 28), p. 208.
[40] O.E. Mogensen, *Positron Annihilation in Chemistry* (Springer-Verlag, Berlin, 1995).
[41] A. Uedono, Z.Q. Chen, R. Suzuki, T. Ohdaira, T. Mikado, S. Fukui, A. Shiota, and S. Kimura, J. Appl. Phys. **90**, 2498 (2001).

[42] G. Dlubek, H.M. Fretwell, and M.A. Alam, Macromolecules **33**, 187 (2000).
[43] S. Dannefaer and D. Kerr, Nucl. Instrum. Methods **131**, 119 (1975).
[44] S. Dannefaer, T. Friessnegg, D. Kerr, A. Uedono, X. Li, and S. Tanigawa, Phys. Rev. B **54**, 15051 (1996).
[45] S.J. Tao, J. Chem. Phys. **56**, 5499 (1972).
[46] M. Eldrup, D. Lightbody, and J.N. Sherwood, Chem. Phys. **63**, 51 (1981).
[47] D.W. Hamby, D.A. Lucca, M.J. Klopfstein, and G. Cantwell, J. Appl. Phys. **93**, 3214 (2003).